aerospace

MDPI

Article

Re-Entry Comparison of a Spacecraft in Low Earth Orbit: Propulsion-Assisted vs. Non-Propulsive Configurations

Antonio Sannino, Dylan De Prisco, Sergio Cassese, Stefano Mungiguerra *, Anselmo Cecere and Raffaele Savino

Department of Industrial Engineering, University of Naples Federico II, P.le Tecchio 80, 80125 Napoli, Italy; antonio.sannino2@unina.it (A.S.); dylan.deprisco@unina.it (D.D.P.); sergio.cassese@unina.it (S.C.); anselmo.cecere@unina.it (A.C.); raffaele.savino@unina.it (R.S.)

* Correspondence: stefano.mungiguerra@unina.it

Abstract: This paper presents a mission concept for a Low Earth Orbit (LEO) satellite equipped with a payload for space experiments, designed to be recovered on Earth post-mission. The focus of this study is on developing a mission concept with fast de-orbit and accurate landing capability for a small satellite payload. Two re-entry configurations are analyzed: one employing a deployable aero-brake heat shield for aerodynamic descent and another integrating a propulsion system. Aerodynamic analysis of the capsule, including drag coefficient and stability at relevant altitudes, was conducted using the Direct Simulation Monte Carlo (DSMC) method. A trade-off analysis, accounting for uncertainties such as C_D, atmospheric density, and ignition timing, revealed significant differences in mission profiles. A propulsion system providing a ΔV of approximately 100 m/s reduces descent time from 54 days (aerodynamic-only re-entry) to under 1 h, without altering trajectory. Drag-related uncertainties contribute to a landing dispersion of ~100 km, while a $\pm 1\%$ error in total impulse increases dispersion to 400 km. A monopropellant rocket engine was preliminarily designed, meeting constraints such as catalytic chamber pressure and performance targets. The resulting thruster, weighing under 4 kg and contained within a 250 mm-high, 350 mm-diameter cylinder, supports three potential component layouts.

Keywords: atmospheric re-entry; landing dispersion; DSMC; monopropellant thruster design

check for updates

Academic Editor: Kyun Ho Lee

Received: 19 December 2024
Revised: 15 January 2025
Accepted: 21 January 2025
Published: 23 January 2025

Citation: Sannino, A.; De Prisco, D.; Cassese, S.; Mungiguerra, S.; Cecere, A.; Savino, R. Re-Entry Comparison of a Spacecraft in Low Earth Orbit: Propulsion-Assisted vs. Non-Propulsive Configurations. *Aerospace* **2025**, *12*, 79. https://doi.org/10.3390/aerospace12020079

Copyright: © 2025 by the authors. Licensee MDPI, Basel, Switzerland. This article is an open access article distributed under the terms and conditions of the Creative Commons Attribution (CC BY) license (https://creativecommons.org/licenses/by/4.0/).

1. Introduction

In recent years, there has been growing interest in designing and implementing small and nano satellites due to their compact size and the availability of standardized components, which reduce the time and cost of building these satellites compared to larger ones [1]. Small and nano satellites are particularly well-suited for low-orbit tasks such as Earth observation and telecommunications. Other applications include scientific experiments or technology, space exploration, Earth observation [2], astrophysics, biology, or physical sciences in microgravity. In all these applications, it may be useful to recover the satellite from space and land it at a specific point on Earth.

The re-entry of bodies from space has been of great interest to many researchers in recent decades [3–6]. A distinction can be made between controlled de-orbiting missions, in which the body is de-orbited and re-enters space at a point on the Earth's surface, and uncontrolled de-orbiting missions, in which one is not interested in recovering the satellite at a specific point (or rather, one ensures that it is destroyed in contact with the atmosphere during descent). To recover the re-entering satellite intact, possible systems to reduce the aerothermodynamic loads acting on the body during descent

can be broadly classified as deployable systems, which include both rigid and inflatable configurations [7–9]. Deployable systems, having been extensively studied [4–6] and recently tested [10], have demonstrated their ability to ensure the safe and controlled reentry of spacecraft. Inflatable systems, as a subset of deployable systems, rely on inflation mechanisms to achieve their operational configuration. In contrast, inflatable systems may present risks of air leaks or malfunctions during deployment or use, potentially making them less reliable under certain circumstances [11,12]. These distinctions highlight the need for careful consideration of mission requirements when selecting rigid or inflatable deployable systems to balance reliability and performance.

Drag sails represent another viable alternative, as demonstrated in prior research [13]. These passive devices utilize atmospheric drag to accelerate the orbital decay of a satellite, enabling re-entry without active propulsion. While drag sails are lightweight and require minimal power, they are prone to damage from sharp changes in thermal conditions during re-entry, which can compromise their effectiveness.

In de-orbit and atmospheric reentry problems, bodies are often encountered moving at altitudes below 400 km, which is within the Very Low Earth Orbit (VLEO) region. At these altitudes, the atmosphere is rarefied, and studying the interaction between the body's surface and the atmospheric environment requires advanced numerical techniques, such as the Direct Simulation Monte Carlo (DSMC) method [14].

Deployable capsules have been extensively studied at the Department of Industrial Engineering, University of Naples Federico II [15–17], with a particular focus on the applicability of fully aerodynamic reentry systems or control devices for propulsive reentries, and also for aerodynamic characterization [18]. However, only in very recent studies have options for the application of thrusters for such vehicles been evaluated [19,20]. While the propulsion system entails the sacrifice of certain enticing features inherent in deployable technology, its implementation offers a strategic avenue for mitigating various challenges associated with aerodynamic control (including de-orbiting time and landing dispersion). Thanks to this, the introduction of a propulsion system may elevate the starting Technology Readiness Level (TRL) of a deployable re-entry system, de-risking an in-orbit validation of this technology. The present work is thus aimed at quantitatively analyzing the reduction in mission uncertainties due to the presence of the propulsion system and obtaining the main requirements for the conceptual design of the thruster.

It is advisable to use chemical rockets over electric propulsion systems, as the latter do not provide sufficient thrust for satellite re-entry [21]. As a safety measure, it is preferable to avoid solid rocket motors, though liquid rocket engines have the drawback of manufacturing complexities and higher inert masses [22]. It is possible to select either hybrid rocket engines [23], for their compact design, safety, and simplified construction, or monopropellant thrusters [24,25]. However, the temperatures in the combustion chamber of hybrid rocket engines (HRE) reach around 2500–3000 K, whereas in monopropellant thrusters, the catalytic chamber's temperature is much lower. Thus, despite the higher specific impulse of HREs for the same thrust, from a thermal perspective, monopropellant thrusters are more manageable. In situations where bulk is not an issue, the lower specific impulse of monopropellant thrusters is not a fatal limitation. One option is to use hydrogen peroxide, which has an ideal decomposition temperature of around 1100 K, which is lower than the combustion temperature of a hybrid rocket engine.

While they offer a simpler design and thermal management compared to hybrid rockets, they are not without limitations. Monopropellant thrusters can exhibit variability in specific impulse due to catalyzer degradation or imperfect decomposition of the propellant. These characteristics must be carefully managed to ensure reliable operation during critical re-entry maneuvers. Moreover, the thrust provided by monopropellant systems may be

limited, which could constrain their applicability for heavier payloads or missions requiring rapid orbital adjustments. Overall, for the intended application, their advantages overcome their drawbacks, and thus monopropellant technology was chosen for this study.

This paper investigates the aerodynamic and propulsion-assisted re-entry of a spacecraft in Low Earth Orbit (LEO). The methods employed include DSMC simulations to characterize the satellite's aerodynamic properties and a conceptual design of a monopropellant thruster tailored to the mission requirements. A comparison between purely aerodynamic versus propulsion-assisted re-entry strategies has been made, highlighting key trade-offs such as descent time, landing dispersion, and thermal loads. The propulsion design leverages a parametric tool to ensure compatibility with geometric constraints while optimizing performance metrics. By synthesizing these analyses, the study offers insights into the practical implementation of combined aerodynamic and propulsion-based re-entry systems, providing a framework for designing future satellite recovery missions.

2. Methods

This section outlines the characteristics of the satellite under study, the reference orbital parameters of the mission, and the numerical setup employed in DSMC simulations to determine the satellite's aerodynamic properties. Additionally, it describes the methods for calculating aerothermodynamic loads during reentry and the preliminary design approach for sizing a monopropellant thruster compatible with maximum geometric constraints.

The satellite, with a total mass of 32 kg (including 4 kg allocated for a potential propulsion unit), is equipped with a deployable heat shield that facilitates reentry by reducing the aerothermodynamic loads. It houses a mini laboratory designed for experiments in a microgravity environment. To ensure reliable results, the rarefied aerodynamics of the capsule at the mission's target altitudes were analyzed in detail using the SPARTA software [26]. This analysis provided the drag coefficient (C_D) profile as a function of altitude and examined the pitch stability of the body in both folded and deployed configurations. Once the aerodynamic characteristics were determined, the General Mission Analysis Tool (GMAT) [27] was employed to evaluate the feasibility of achieving a purely aerodynamic reentry at a specific point on the Earth's surface. The analysis demonstrated how uncertainties in parameters such as the drag coefficient and atmospheric density introduce dispersion in landing and significantly influence the mission profile. The application of propulsion to reduce the reentry time is analyzed, and it is shown that for the same parameters, the dispersion at landing is generally smaller. The mission requirement for the ΔV needed for reentry has been identified. In conclusion, a conceptual design of a suitable monopropellant rocket capable of providing the required ΔV, obtained using an in-house developed parametric tool, is presented. The combined use of these tools enables the accurate design of space missions for Low Earth Orbit (LEO) and Very Low Earth Orbit (VLEO).

2.1. Satellite and Orbit Configurations

In Table 1, the satellite's reference orbit data and geometrical characteristics are presented. The satellite falls into the small-satellite category, and a low polar orbit (altitude ~400 km, inclination 98°) was selected. Figure 1 illustrates the satellite's geometry (Figure 1a) and the reference frame used for the pitch stability study (Figure 1b), with the z-axis pointing outward and the moments being positive in the clockwise direction. Figure 1c shows the body reference frame (subscript B), highlighting the direction of the change in velocity applied by the monopropellant thruster. Table 1 also lists the reference areas used to calculate the aerodynamic coefficients of the satellite in its folded and deployed configurations. For the calculation of the pitch moment coefficient, the diameter of each configuration was chosen as the reference length. The moments are calculated consider-

ing the center of gravity at x_{cg} = 0.34 m, y_{cg} = 0, z_{cg} = 0 for the deployed configuration, corresponding to approximately 0.25 times the heat shield diameter, while for the folded configuration, the center of gravity was assumed at x_{cg} = 0.5 m, y_{cg} = 0, z_{cg} = 0, taking into account the possibility of a shift along the x-axis when transitioning from the folded to deployed configuration.

Table 1. Satellite and initial orbit reference data.

Semi-major axis	6778 km
Eccentricity	0.000776
Inclination	98°
Right ascension of ascending node	225°
Argument of perigee	0°
True anomaly	0°
Dry mass of satellite without propulsion system	28 kg
Total mass of propulsion system	4 kg
Drag area	0.125 m^2 (folded), 1.5 m^2 (deployed)
Diameter	0.398 m (folded), 1.382 m (deployed)
Curvature radius	0.3 m

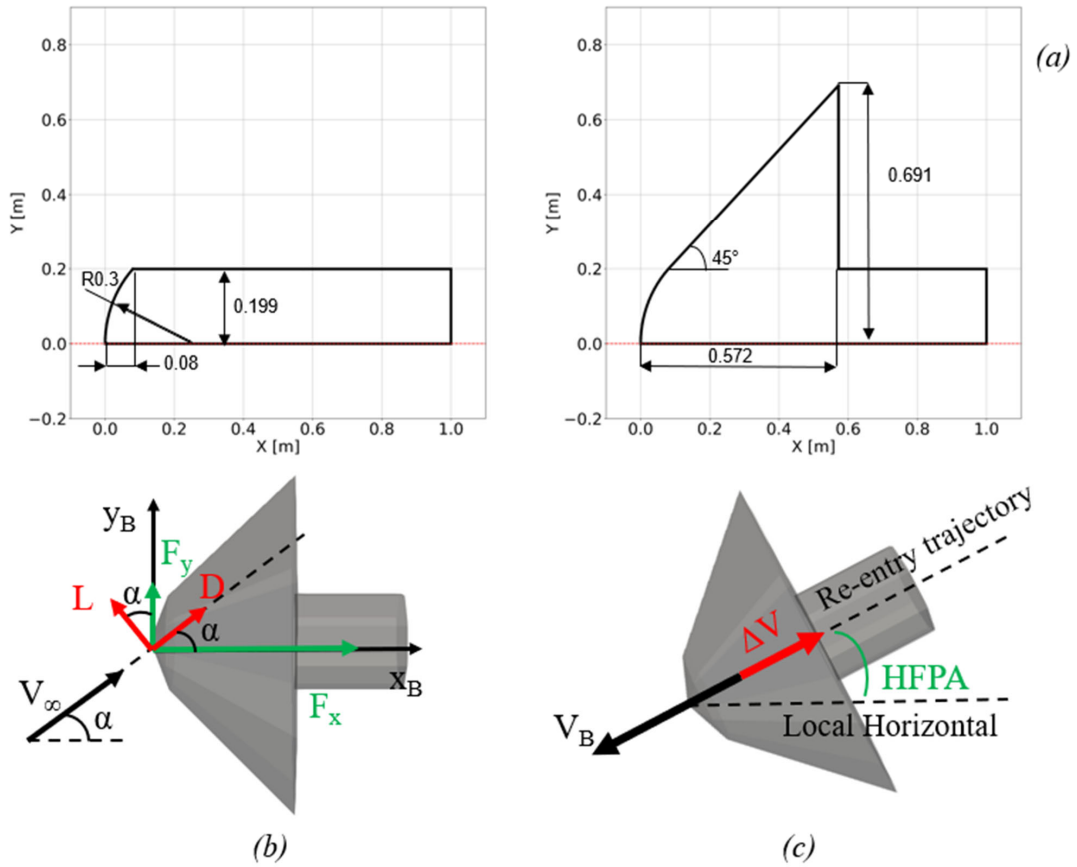


Figure 1. Geometric characteristics of satellite: (**a**) folded configuration (on the left), and deployed configuration (on the right), (**b**) reference frame for DSMC simulations, (**c**) reference frame for propulsive reentry.

2.2. Numerical Set-Up for DSMC Calculations

To determine the aerodynamic characteristics of the satellite in the rarefied flow regime, the domain shown in Figure 2 was considered, extending 12 m in the direction of velocity and 3 m in the perpendicular direction. The geometry is axisymmetric, and far-field conditions were set using data provided by [28], as shown in Table 2, based on the MSISE-90 atmospheric model, which is included by default in the GMAT library. The mean free path of the asymptotic flow, λ_∞, was calculated using Equation (1), where the reference diameter is the mass-weighted average of the diameters of the individual species, R is the gas constant, k_B is the Boltzmann constant, N_A is Avogadro's number, and N_∞ is the number density of the free stream. The mesh used for the 2D axisymmetric simulations to determine the C_D vs. Altitude profile consists of three levels: level 1 with cell sizes of approximately 8 cm, level 2 with cell sizes of approximately 4 cm, and level 3 with cell sizes of approximately 2 cm. Additionally, a wall refinement is implemented with cells of approximately 1 cm in size.

$$\lambda_\infty = \frac{k_B N_A}{\sqrt{2}\pi\, R\, d_{ref}^2\, N_\infty} \tag{1}$$

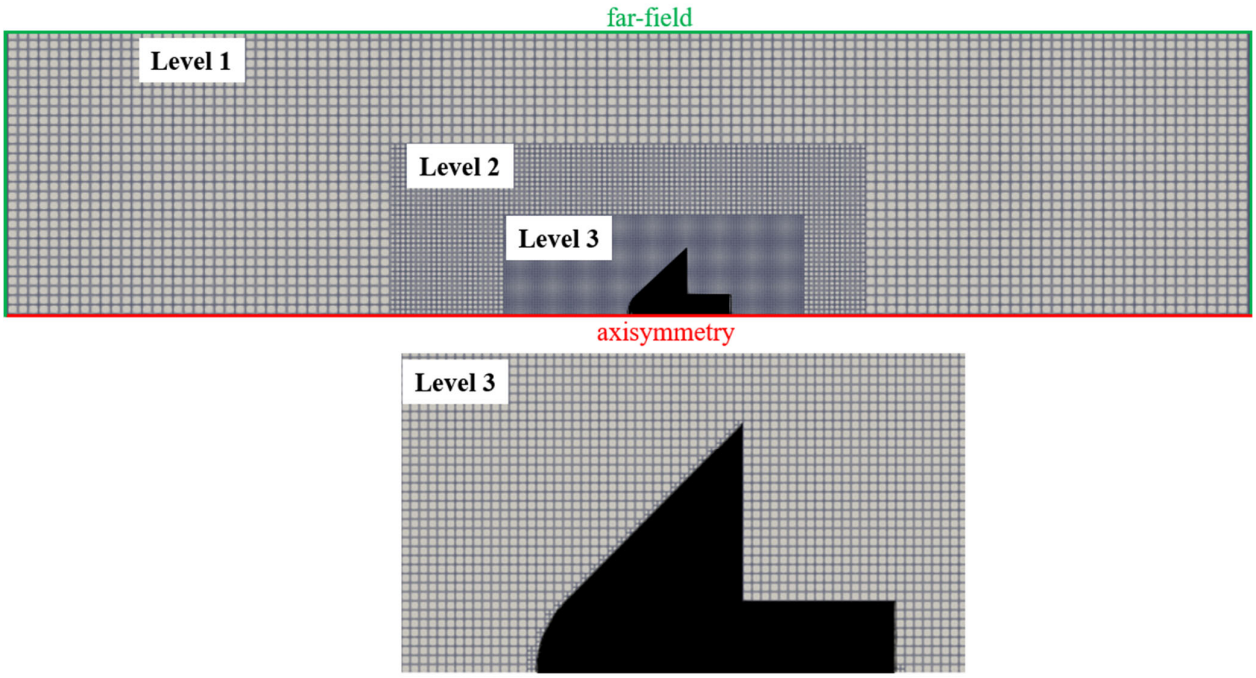


Figure 2. Calculation grid with three refinement level and detail on the body surface.

For the pitch stability study, the domain was extended into a 3D box, limited to the dimensions of level 2 (x, y, and z ranging from -2 m to 2 m). The chosen time-step is 1×10^{-7} seconds to ensure that the particle travels no more than 1/3 of the cell size in the most refined region, for both the 2D and 3D simulations.

As demonstrated in [29], the selection of the Gas Surface Interaction model and the associated accommodation coefficient are paramount for precise force prediction. To simulate the interaction between the flow particles and the wall, the Maxwellian model is employed, with a fully diffuse reflection obtained setting the accommodation coefficient (defined in Equation (2)) to 1. In Equation (2), the E_i represents the kinetic energy of the incident particle, E_r denotes the energy of the re-emitted particle, and E_w signifies the energy the particle needs to deplete to reach thermal equilibrium with the wall [30,31]. The

wall is isothermal at a temperature of 300 K, and any incident particle fully accommodates to the wall before being re-emitted.

$$\alpha_{acc} = \frac{E_i - E_r}{E_i - E_w} \tag{2}$$

Table 2. Atmospheric data from MSISE-90 model [28].

Altitude [km]	Number Density Fraction			Number Density [1/m^3]	Temperature [K]	Velocity [m/s]	λ_∞ [m]
	N_2	O_2	O				
100	0.788	0.176	0.036	1.45×10^{19}	170	7850	0.1
120	0.731	0.076	0.193	4.60×10^{17}	382	7840	3
160	0.579	0.034	0.387	3.45×10^{16}	862	7810	47
180	0.513	0.027	0.459	1.75×10^{16}	968	7800	98
210	0.422	0.020	0.559	7.85×10^{15}	1054	7780	232
240	0.338	0.014	0.648	4.00×10^{15}	1093	7760	485
270	0.265	0.010	0.725	2.19×10^{15}	1111	7750	935
300	0.204	0.007	0.789	1.26×10^{15}	1120	7730	1700

2.3. Models for Orbital Propagation and Aero-Thermodynamic Loads Evaluation

Utilizing NASA's GMAT (General Mission Analysis Tool) enables the thorough exploration of space missions with a highly precise orbital propagator that takes into consideration the influence of multiple perturbations [27].

In this work, the following assumptions were made:

- Earth Gravity Model: EGM-96, gravitational harmonics up to order and degree 100.
- Solar Radiation Pressure: spherical model, geomagnetic and solar activity given by GMAT database.
- Atmospheric model: MSISE-90, spherical model.
- Third body: Sun, Moon.
- Integrator: Runge-Kutta 89, accuracy 10^{-8}.

This model does not account for aerodynamic lift; however, this does not compromise the validity of the comparison between the two re-entry strategies (aerodynamic and propulsive) presented herein.

For the evaluation of the aerothermodynamic loads, Newton's approximate theory was used to study the gas-surface interaction in the rarefied regime and to determine the pressure acting on the satellite (Equation (3)).

$$P_0 = \frac{1}{2}\rho V^2 C_p \tag{3}$$

where C_p is equal to 2 by Newton's approximate theory [32,33].

For the wall temperature and heat flux, engineering models were considered as shown in [33–35] and, for simplicity's sake, below:

$$\dot{q_0} = 1.83\ 10^{-4}\sqrt{\frac{\rho}{R_c}}V^3 \tag{4}$$

The Equation (4) represents the Tauber's formula, where ρ is the atmospheric density, R_c the curvature radius of the nose, and V is the flight speed. In Tauber's formulation

(Equation (5)), the heat flux is calculated under the assumptions of steady hypersonic flow, treating the body as moving within a continuum regime and neglecting significant radiative effects.

The radiative equilibrium temperature profile corresponding to the convective heat flux computed at the stagnation-point can be calculated by solving, with respect to the wall temperature T_w, the quartic Equation (5). The equation has been solved by means of Newton's method, with c_p being the specific heat (equal to 1000 J/kg K in this work), σ being the Stefan-Boltzmann constant, and ε being the surface emissivity. For the radiative equilibrium temperature calculation (Equation (5)), it is assumed that the surface behaves as a gray body, with constant emissivity (equal to 0.8) and neglecting transmission effects. The calculation is constrained to radiative equilibrium conditions, excluding thermal conduction and transient effects, and the wall is assumed as fully catalytic.

$$\dot{q_0}\left(1-\frac{c_p T_w}{\frac{V^2}{2}}\right)-\sigma\epsilon\, T_w^4=0 \tag{5}$$

2.4. Method for Thruster Design and Parametrization Process

A computational tool was developed to simulate the thermochemical performance of high-concentration hydrogen peroxide (HTP) monopropellant rockets and recommend optimal thruster sizes. The model, based on thermodynamic principles and conservation laws, ensures scalability beyond the validated range and operates independently of external software like NASA CEA [36]. It calculates theoretical performance by assuming stoichiometric dissociation of hydrogen peroxide and adiabatic energy transfer to propulsion [37]. The tool was validated for HTP concentrations between 70% and 98%, showing results consistent with NASA CEA simulations. These findings demonstrate the tool's reliability for predicting rocket performance.

For the propulsion system sizing, a preliminary study of a space mission is necessary to determine the requirements. The design procedure involves sizing individual subsystems according to references [38–40]. The tool implements an optimization process based on expansion ratio and constraints of mass and volume. Specifically, the tool calculates the thruster performance and designs components for expansion ratio ranging from 2 to 200. Among all possible solutions satisfying the performance requirements, for the three configurations presented in the final section of this work, the one with an expansion ratio that ensures components have dimensions compatible with the satellite and minimizes the total mass of the propulsion system is selected.

The following Figure 3 presents a schematic representation of the components to be sized for a monopropellant thruster.

The specific impulse (I_{sp}) determines the propellant flow rate, which can be derived from Equation (6) by selecting a thrust value:

$$\dot{m}=\frac{T}{I_{sp}g_0} \tag{6}$$

The ΔV is related to the propellant mass by the Tsiolkowskij equation (Equation (7)):

$$\Delta V = c\ln\left(\frac{m_i}{m_i-m_p}\right) \tag{7}$$

Moreover, it is possible to write (Equation (8)):

$$I_{tot}=m_p\, c = T\, t_b \tag{8}$$

where m_i is the total mass of satellite, m_p is the propellant mass, c is the effective exhaust velocity, T is the thrust, t_b is the burning time, I_{tot} is the total impulse, and ΔV is the velocity change. By choosing a value for the thrust, calculated the total impulse from propellant mass and the selected effective exhaust velocity, it is possible to calculate the burning time.

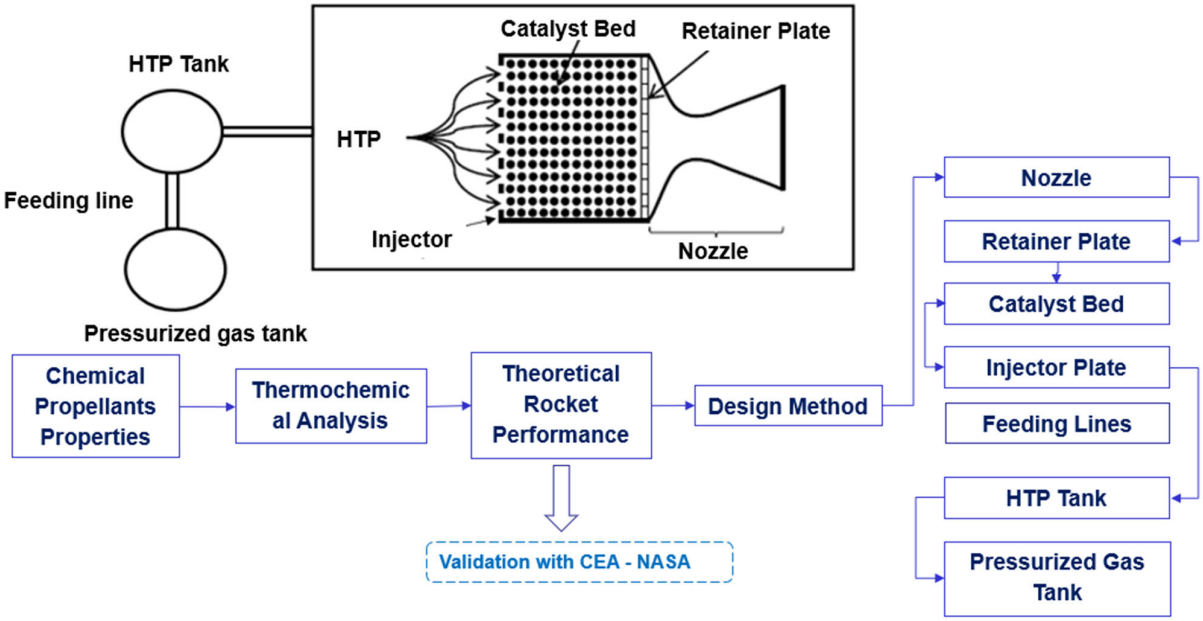


Figure 3. Monopropellant thruster simplified scheme [23] and schematic summary of rocket performance calculation and thruster design procedure.

3. Results

In this section, the main results of the study are presented. Initially, the results of the DSMC simulations to determine the satellite's aerodynamics are shown. Subsequently, a comparison between aerodynamic re-entry and propulsive re-entry is conducted, highlighting the key differences between the two methods. Finally, the design of the propulsion system for performing the re-entry is presented.

3.1. DSMC Results

Axisymmetric 2D simulations were conducted to determine the drag coefficient (C_D) profile as a function of altitude under the assumption of zero angle of attack relative to the flow. Density and velocity contours in Figure 4 illustrate the thinning of the shock layer as the satellite descends from 300 km (altitude traversed during descent) to 120 km (conventional reentry interface) for both folded and deployed configurations. This effect is attributed to the decreasing flow rarefaction and the transition regime (Knudsen number ~1). The pitch moment coefficient versus angle of attack (Figure 5d) reveals passive stability in both configurations, with the satellite tending to return to the equilibrium position (α = 0) as the angle of attack increases. The stability range extends from 0° to 60° in the folded configuration and 0° to 45° in the deployed configuration. Consequently, it is reasonable to assume that during the mission, the capsule will maintain an angle of attack near equilibrium (α = 0), where the lift coefficient (C_L, Figure 5c) is negligible compared to the drag coefficient (C_D, Figure 5b). For orbital propagation in this study, C_L is disregarded. The C_D value at altitudes between 300 km and 400 km is taken as the DSMC result at 300 km, while below 100 km, a C_D of 1 is assumed, as suggested in [31]. For the altitude range between 300 km and 100 km, the profile obtained with linear interpolation of the data points shown in Figure 5a is used, depending on whether the satellite is in the deployed or folded configuration. Specifically, during propulsive re-entry, the satellite remains in the

deployed configuration from 300 km down to 0 km. In the case of aerodynamic re-entry, the satellite transitions between configurations: it is in the deployed configuration from 300 km to 230 km, in the folded configuration between 230 km and 210 km, and then returns to the deployed configuration from 210 km down to 0 km.

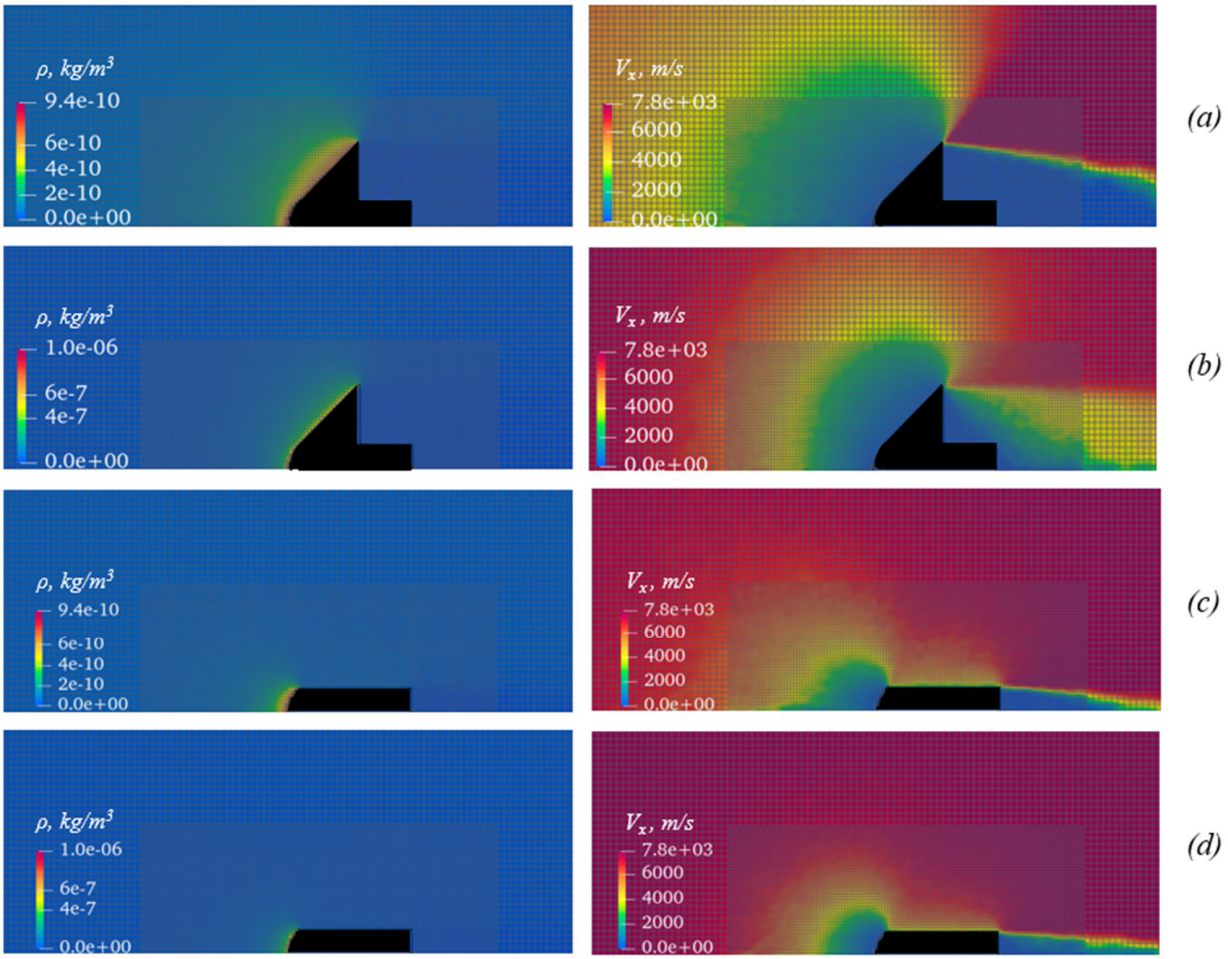


Figure 4. Density contours (**left**) and velocity contours (**right**) for the satellite are shown in the deployed configuration at 300 km (**a**) and 120 km (**b**) altitudes, as well as in the folded configuration at 300 km (**c**) and 120 km (**d**) altitudes.

Furthermore, for a zero angle of attack, the drag force is significantly greater than the lift force in both the folded and deployed configurations, and this is in accordance with the assumption of neglecting the lift. Additionally, from the static pitch stability analysis, it is shown that for a zero angle of attack, the pitching moment coefficient derivative C_{M_α} is negative in both configurations. This ensures that, in a preliminary design phase, lift can be neglected as the capsule naturally stabilizes around a zero angle of attack. As [41] observes, static stability does not preclude dynamic stability concerns. A dynamic pitch stability analysis could further confirm the stability of the zero angle of attack configuration; however, such an analysis falls outside the scope of this preliminary design phase. Moreover, a sub-orbital flight of a 45 degrees semi-aperture capsule showed static and dynamic stability in all flight regimes, including transonic [10].

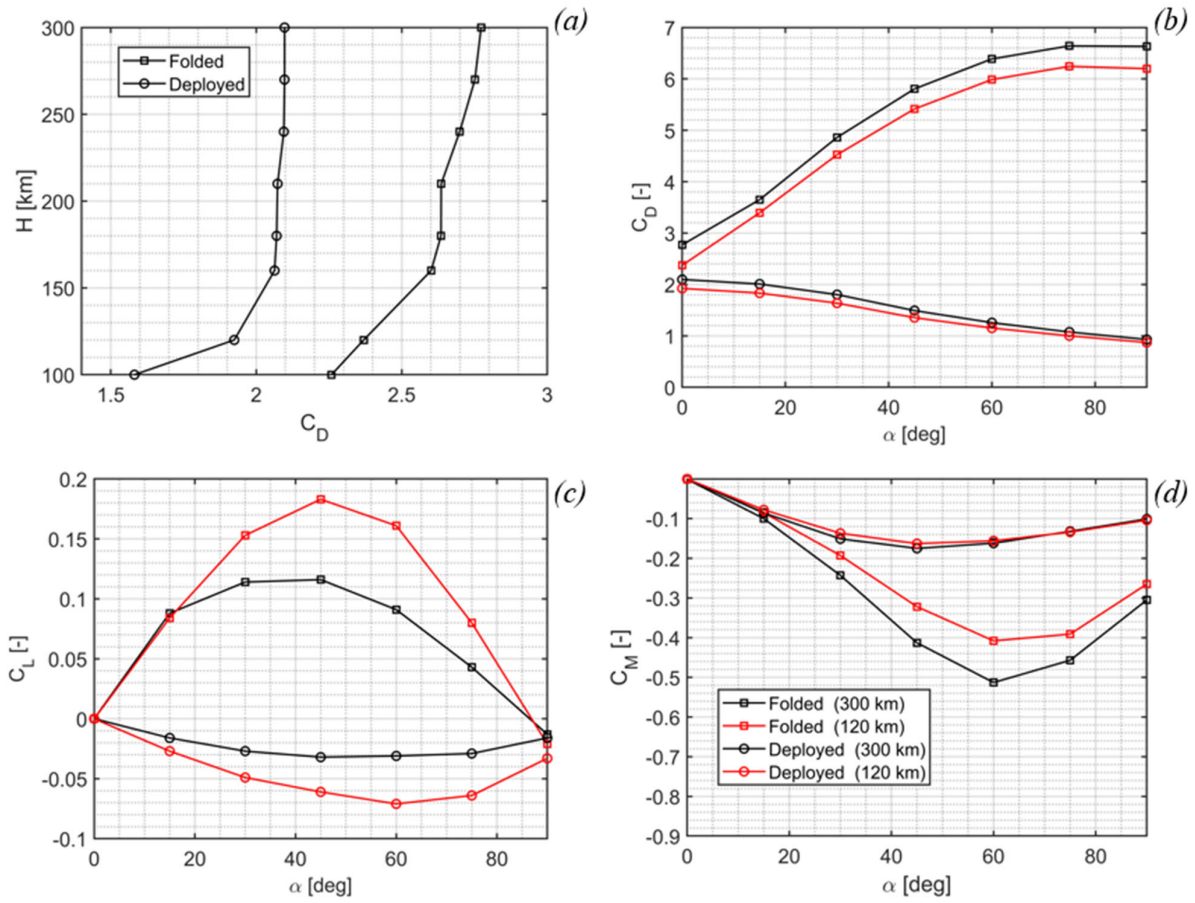


Figure 5. Aerodynamic Study Results: The variation of C_D with altitude for zero angle of attack (**a**), the variation of C_D with α (**b**), C_L with α (**c**), and C_M with α (**d**) in both configurations at altitudes of 120 km and 300 km (deployed: x_{cg} = 0.34 m, y_{cg} = 0, z_{cg} = 0; folded: x_{cg} = 0.5 m, y_{cg} = 0, z_{cg} = 0).

3.2. Analysis of Aerodynamic Re-Entry

One possible re-entry strategy is not to use a thruster but, by increasing the surface area of the satellite and decreasing it appropriately, it is possible to land at a precise point on the Earth's surface. The satellite has the characteristics shown in Figure 1 and Table 1, and a total mass of 32 kg is considered (i.e., the 4 kg mass provided for the propulsion module is now considered as a mass that increases the payload). The mission sequence is as follows:

- The satellite orbits for 15 days for the experimental phase;
- After 15 days, the deployable aerobrake is deployed, increasing the reference surface and thus the resistance acting on the satellite, which begins to de-orbit;
- At an altitude of 230 km, the deployable aerobrake is folded to slow down the descent and wait for the right ground-track to return to the target point;
- After a certain waiting time, the deployable aerobrake is opened again to reach the desired point.

In the nominal case of C_D (reported in Figure 5a) and nominal density profile obtained by GMAT database (for the start mission data), the mission sequence specifically is as follows:

- 15 days of propagation for the experimental phase; then, the descent phase with the deployable aerobrake open begins until an altitude of 230 km is reached on 20 February 2024
- Satellite orbits for 3 days and 21,545 s with deployable aerobrake closed

- In data 23 February 2024 (6:00 AM), the deployable aerobrake is open, at the altitude of ~ 210 km
- In data 23 February 2024 (6.00 PM), the satellite achieves the landing point 48.70° S, 123.01° W.

Figure 6 shows the altitude profile with respect to the time obtained from GMAT. The oscillation in altitude over time is related to the orbital eccentricity (reported in Table 1) and the oblateness of the Earth.

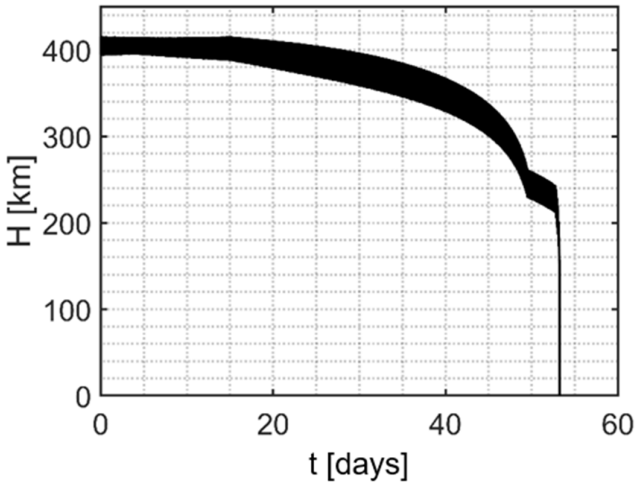


Figure 6. Altitude profile (in km, y-axis) with respect to the time (in days, x-axis) (start date 1 January 2024).

3.3. Propulsive Re-Entry: ΔV Selection, Thrust Determination, Mission Description and Results

This section discusses the use of a propulsive action to aid in the reentry of a satellite. The satellite is in orbit for 15 days to conduct experiments. After a waiting period to ensure the satellite follows the correct ground-track for reentry at the desired landing site, a change in velocity is applied in the direction opposite to motion.

Using GMAT, it is possible to set up the mission, which is structured in the following sequence:

- The satellite is in orbit for 15 days at an altitude of 400 km where experiments are conducted.
- Waiting phase (3 days and 17,005 s) to individuate the ground track to re-enter close to the co-ordinate point 49.43° S, 123.77° W.
- Application of propulsive burn.
- Once the altitude of 300 km is reached, the umbrella is deployed to facilitate re-entry and reduce the aerothermodynamic loads acting on the satellite.
- Impact on the Earth surface close to the point 49.43° S, 123.77° W.

The timing of the waiting phase for the burn application in propulsive re-entry and aerobrake folding and unfolding in aerodynamic re-entry is determined based on a simplified strategy that relies on the initial orbital parameters and the target landing location to predefine the sequence of maneuvers. Therefore, the variation in waiting times between different strategies should not be surprising.

The GMAT software can be used to calculate the ΔV required for a satellite to reach the reentry interface, which is typically set at an altitude range of 100–125 km. In this case, an impulsive ΔV of 86 m/s is sufficient for the satellite to successfully reenter. For lower values, the satellite does not immediately penetrate the atmosphere; instead, it reaches an altitude of 115 km, which then slightly increases. However, thanks to aerodynamic drag, it still achieves a point on the Earth's surface. Figure 7 illustrates this process.

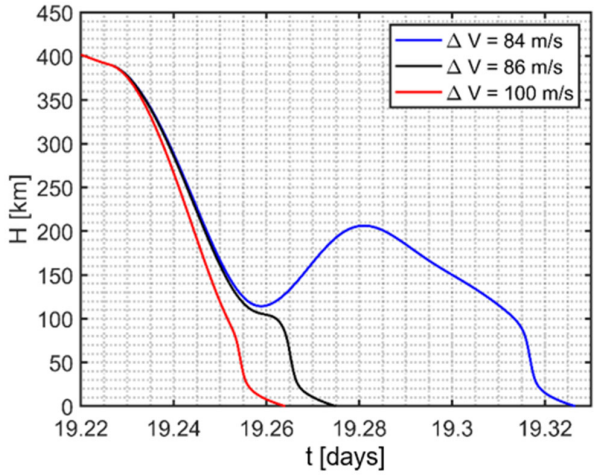


Figure 7. Altitude w.r.t. time for different change in velocity provided.

A ΔV value of 100 m/s was selected from the possible values greater than 86 m/s. The objective is to re-enter a specific point on the Earth's surface with a re-entry angle γ of approximately 1 degree at an altitude of 100 km. An ΔV of 100 m/s results in a Horizontal Flight Path Angle (HFPA) of 0.8 degrees, while a value of 90 m/s results in an HFPA angle of 0.3 degrees, and 120 m/s results in an HFPA angle of 1.43 degrees (as summarized in Table 3). A change in velocity of 100 m/s was selected for the mission sequence, which involves a propulsive burn ensuring a landing at point 49.43° S, 123.77° W.

Table 3. Horizontal Flight Path Angle (HFPA) at 100 km for different ΔV applied.

ΔV [m/s]	HFPA at 100 km
90	0.30°
100	0.80°
120	1.43°

In this work, a finite burn with a monopropellant engine is planned. Specific impulse in vacuum can be calculated as 150 s by considering hydrogen peroxide (wt% 91), under preliminary assumptions, using CEA [36] and assuming an overall efficiency of 90%, an Expansion Ratio of 15, and a chamber pressure of 10 bar. In Table 4, a summary of data is shown. If a thruster capable of providing a thrust of 50 N is assumed, the flow rate can be calculated using Equation (6) and is equal to 33.98 g/s.

Table 4. Summary of input and output data for using CEA [36].

Input Parameter	Value
H_2O_2 wt%	91
Overall efficiency %	90
Expansion Ratio	15
Chamber Pressure	10 bar
Output parameter	**Value**
I_{sp}	150 s

Choosing a value for the thrust, calculated by the total impulse with RPA, the propellant mass flow rate is determined, and, from the effective exhaust velocity, it is possible to calculate the burning time by combining Equations (7) and (8). For the given data, to

obtain a mean change in velocity of about 100 m/s, a total impulse of 3100 Ns was applied, with roughly 2.1 kg propellant consumption. Table 5 compares the effects of applying a thrust of 25 N, 50 N, or 100 N for the same total impulse. At an altitude of 100 km, the HFPA consistently measures 0.8 degrees. However, there is a dispersion upon landing that is presumably related to the variation in the satellite position during the burning time (summarized in Table 5). For this study, an intermediate scenario was chosen so that the burn would not last too long (25 N for 124 s would require the system to operate at a temperature of 1000 K) and the thrust value would not be too high (100 N, if not acting along the center of mass, could lead to moments that the inertial wheels could not balance). Assuming that the satellite has wheels of compatible size for inertia and balancing moments in the order of tenths of Newtons x meters, a 1 mm misalignment of the thrust axis from the barycentric axis in any direction would result in 0.025 Nm, 0.050 Nm, and 0.1 Nm of torque, respectively, for 25 N, 50 N, and 100 N. Supposing that 0.3 Nm can be balanced, it is observed that the maximum allowable misalignment decreases from 12 mm at 25 N thrust, to 6 mm at 50 N, and to 3 mm at 100 N. At this pre-design stage, to maintain a maximum misalignment requirement of at least 5 mm and not to expose the satellite structure to high temperatures for too long (excluding the burn time of 124 s), a thrust value of 50 N for an operating time of 62 s is chosen as a compromise. Figure 8 shows the altitude versus time profile in the nominal case.

Table 5. Landing site obtained for different burning conditions.

Conditions	HFPA at 100 km	Latitude at 0 km	Longitude at 0 km
Thrust 25 N, burning time 124 s	0.8°	47.62° S	124.48 W
Thrust 50 N, burning time 62 s	0.8°	49.43° S	123.77 W
Thrust 100 N, burning time 31 s	0.8°	50.32° S	123.41 W

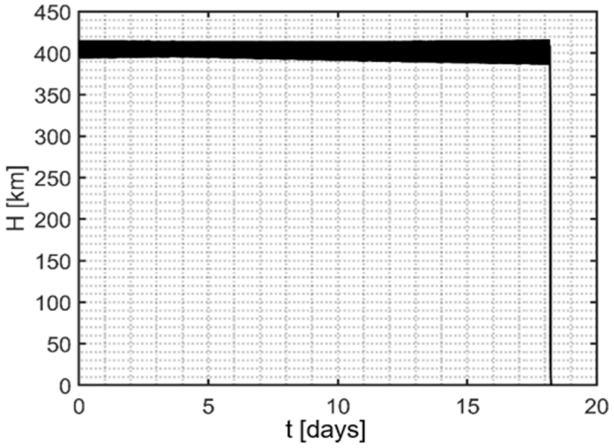


Figure 8. Altitude (in km, y axis) vs. time (in days, x axis) (obtained by GMAT).

Compared to the purely aerodynamic reentry data in Table 6, the maximum pressure and acceleration in this case are lower due to the smaller mass at reentry, resulting in a smaller ballistic parameter. The speed of the body and the atmospheric density during descent plays a key role in heat flux and wall temperature, and since the velocity is greater in the propulsive re-entry, the peak heat flux and wall temperature will also be greater for this case. In conclusion, it is important to notice the difference in the time of descending in the two possible scenarios considered, which affect the landing dispersion as reported in following sections.

Table 6. Density, HFPA at 100 km altitude, speed and maxima values of aero-thermodynamic loads experienced by the satellite, and relative altitudes for the two re-entry strategies.

	Aerodynamic Re-Entry	**Propulsive Re-Entry**
Maximum stagnation pressure	3.2 kPa at 62.5 km	2.9 kPa at 64.7 km
Maximum acceleration/g_0	−7.52 at 62.5 km	−7.33 at 64.7 km
Maximum wall temperature	1804 K at 76.3 km	1818 K at 78.9 km
Maximum heat flux	480 kW/m^2 at 76.3 km	496 kW/m^2 at 78.9 km
Density value at altitude of maximum wall temperature and heat flux	3.54×10^{-5} kg/m^3	2.84×10^{-5} kg/m^3
Density value at altitude of maximum acceleration and stagnation pressure	2.53×10^{-4} kg/m^3	2.21×10^{-4} kg/m^3
Speed at altitude of maximum wall temperature and heat flux	6421 m/s	6718 m/s
Speed at altitude of maximum acceleration and stagnation pressure	3571 m/s	3666 m/s
Speed at 100 km	7839 m/s	7959 m/s
HFPA at 100 km	−0.82 deg	−0.4 deg

The maxima of heat flux and wall temperature are calculated under the assumption of radiative equilibrium, emissivity of 0.8, and results in slightly high values (Equations (4) and (5) from [33–35]). The significant levels of temperature calculated are, however, a very conservative estimate, since thermal conduction and transient effects are neglected. However, research is already studying materials able to survive such high thermal loads [42]. These high-temperature materials have been demonstrated to withstand the calculated thermal loads, ensuring the structural integrity of the spacecraft during re-entry. Therefore, it can be concluded that, under the assumptions and conditions considered, the satellite is expected to successfully survive the re-entry process and land intact.

3.4. Analysis of Main Parameters Variations

Once the order of magnitude of aerodynamic loads experienced by the satellite during the re-entry and the different descending time between the two strategies were understood, an analysis of the density and drag coefficients variations was conducted. The variation of +/−10% with respect to the nominal scenario of these two parameters has been considered for the two strategies. The selection of this range of +/−10% is grounded in the findings of preceding studies [43–46], which substantiate the error on the atmospheric density. With regard to the C_D, there is the consideration of oscillation around the null attitude, resulting in the variation of aerodynamic resistance, or uncertainties in the accommodation coefficient, which may not be equal to 1. Alternatively, there is the option of regarding the re-emission model as non-Maxwellian, in which case reference could be made to the Cercignani–Lampis–Lord value (CLL) [47–49], for which slightly divergent values are demonstrated in [50]. In addition, in the case of propulsive re-entry, a maximum error of +/−10 s on ignition instant and +/1% on total impulse applied has been analyzed.

3.4.1. Influence of Drag Variation on Aerodynamic Re-Entry

Applying the aerodynamic re-entry strategy, the main force acting on the satellite, except for gravity, is the aerodynamic drag, which depends on the density and drag coefficient. The variation on the mission profile due to atmospheric density value and the

C_D value is evaluated. The density profiles considered are obtained from GMAT, setting the atmosphere scale factor equal to 0.9 and 1.1 (in the nominal conditions the atmosphere scale factor is equal to 1). Equivalently, the effects of varying the C_D by $+/-10\%$ from the nominal profile considered in Table 1 are evaluated. The variations are applied after the 15 days of propagation for the experimental phase. This assumption provides an approximation of the results while not affecting the generality of the findings.

With respect to the mission sequence described in the previous section, in Figure 9, it is possible to see the different profile altitude with respect to time due to the density (C_D) variations. Finally, the variation of the aero-thermodynamic loads is shown in Figure 10. It can be observed that higher values of the modified ballistic parameter (given by Equation (8)) result in heavier aerodynamic loads at the altitude where the peak loads are recorded. In Equation (9), ρ is the atmospheric density, C_D is the drag coefficient, S is the drag area, which is the surface of the satellite in the deployed configuration, and m_f is the mass of the satellite during the descent in the final part of the mission, which is equal to the initial mass in the case of aerodynamic re-entry, while in the case of propulsive re-entry, this is reduced by the propellant consumption.

$$B^* = \frac{m_f}{\rho\, C_D S} \tag{9}$$

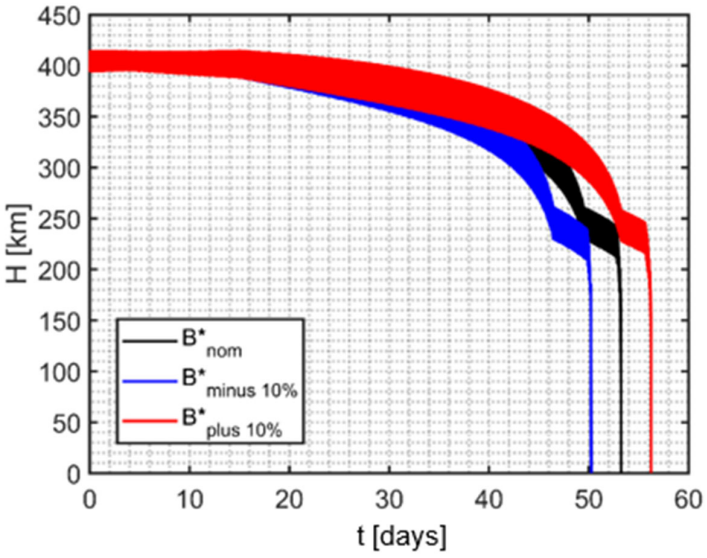


Figure 9. Altitude trends for the different B* considered (aerodynamic re-entry). The B* variation results in significant missions' profile deviations.

It is observed that variations considered for this type of re-entry result in significant changes in the altitude profile over time. The ground track followed in the terminal part of the re-entry is shifted from that of the nominal profile. These changes are reflected at the landing point, causing a dispersion of about 400 km. It should be noted that in order to land in the proximity of the landing-site obtained in the nominal case, the time it takes the satellite to get to an altitude of 230 km, where the deployable heatshield is closed, and the waiting time to deploy the heat shield again, changes. So, to re-enter close to the nominal point, a real-time control strategy is needed that, based on the satellite's navigation state, can act on the surface and the waiting time, which is significantly complex.

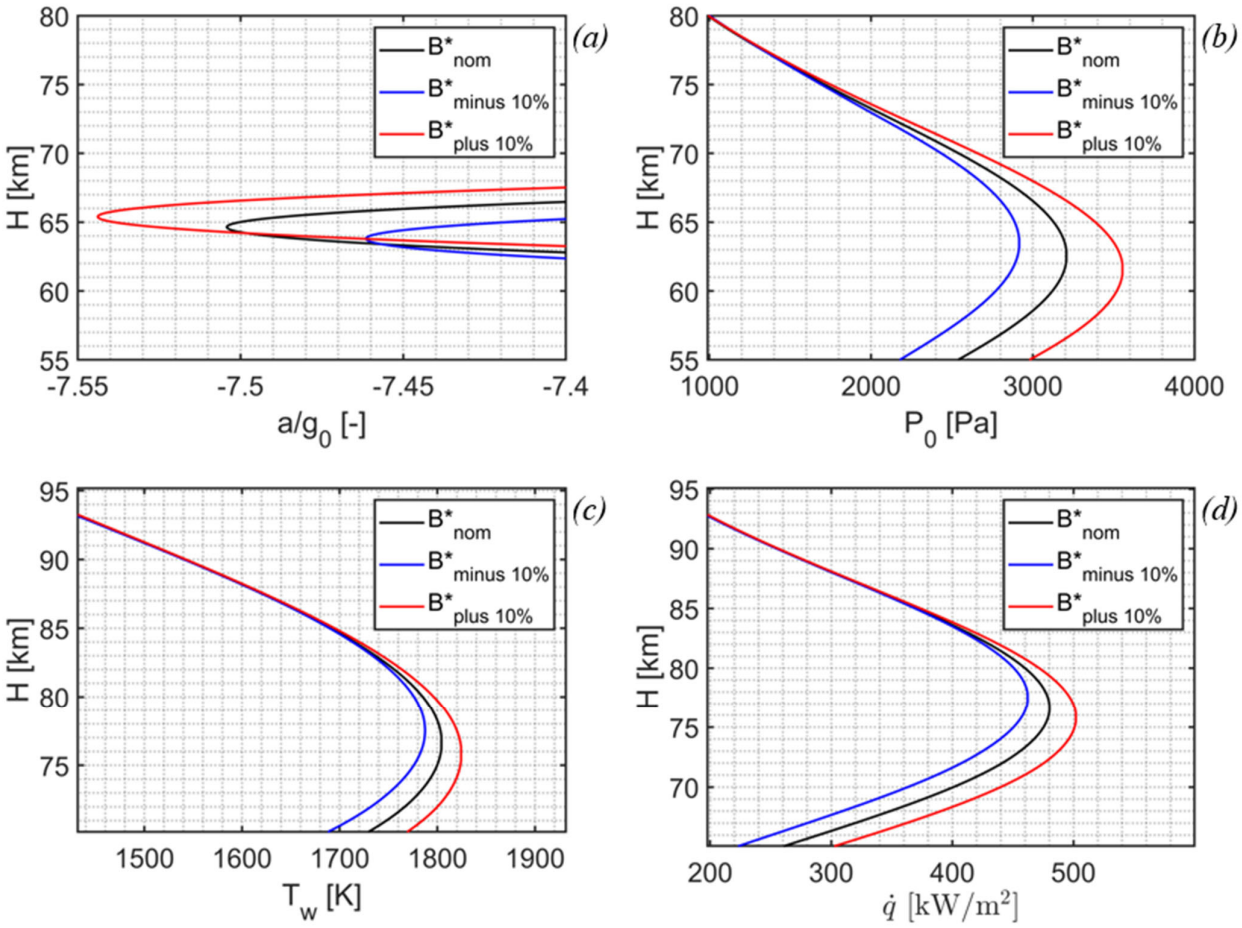


Figure 10. Trend of aerothermodynamic loads during re-entry; (**a**) acceleration, (**b**) pressure, (**c**) wall temperature, (**d**) heat flux (for uncertainty on B*, aerodynamic re-entry).

3.4.2. Influence of Drag Variation for Propulsive Re-Entry

To evaluate the effect of different density and C_D values, the variation considered in the aerodynamic case has been considered. The trends of the aero-thermodynamic loads obtained and the landing dispersion are shown below (Figures 11 and 12, respectively), leaving the nominal mission sequence of propulsive re-entry unchanged. The peaks of the aero-thermodynamic loads depend on B*, as previously observed.

Applying a propulsive action, considering the same perturbations in terms of C_D and density, insignificantly changes the altitude versus time profile, and the satellite will follow a ground track near to the nominal during the terminal phase of re-entry. The maximum dispersion on landing is about 80 km, and the small descending time facilitates potential control actions that allow the body to re-enter near the nominal landing site because the satellite will follow, approximately, the same ground track.

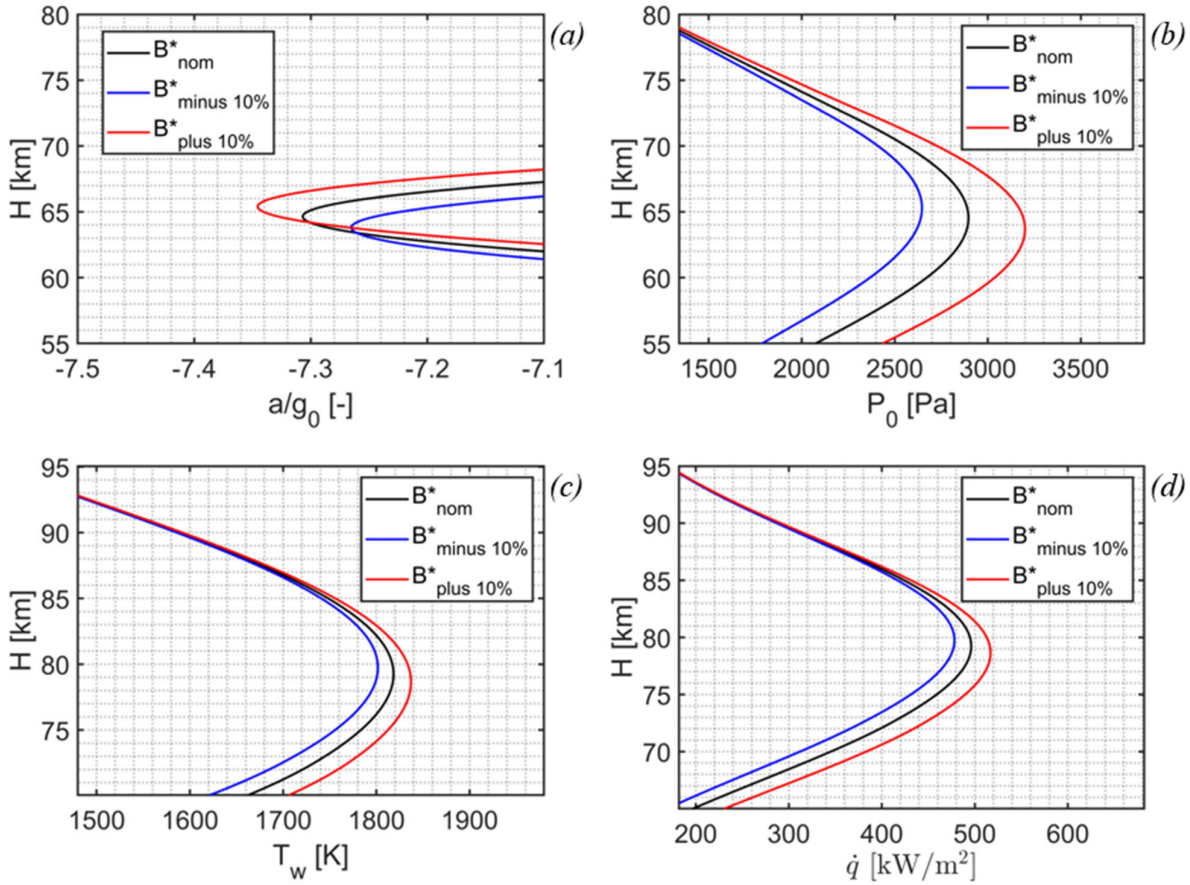


Figure 11. Trend of aerothermodynamic loads during re-entry; (**a**) accelerations, (**b**) pressures, (**c**) temperature, (**d**) heat flux (for different B*, propulsive re-entry).

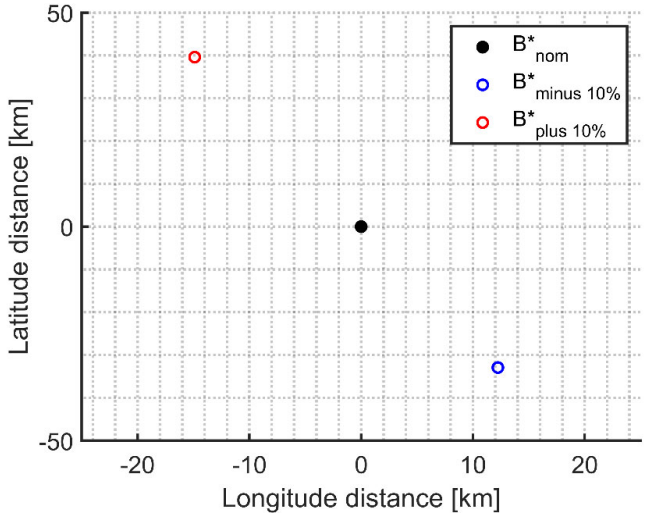


Figure 12. Landing dispersion obtained for different B* (propulsive re-entry).

3.4.3. Influence of the Ignition Instant

The difference in ignition instant does not affect the aerothermodynamic loads, only the landing dispersion. Figure 13 shows the landing dispersion for ignition time errors of +/−10 s.

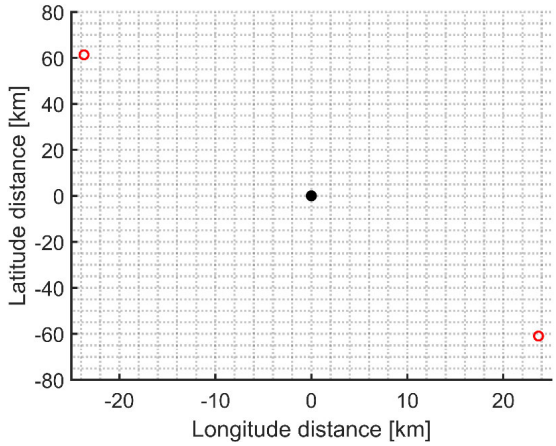


Figure 13. Landing dispersion obtained due to errors on ignition time of $+/-10$ s.

3.4.4. Influence of Total Impulse Applied

One error that could be considered concerns the burning time or, equivalently, the thrust provided. These errors afflict the value of total impulse and thus the ΔV applied to the satellite. An error of $+/-1\%$ on the burning time is considered ($+/-0.62$ s on the burning time, or $+/-0.5$ N on the nominal thrust of 50 N). In addition, providing a larger or smaller ΔV affects the mass of propellant consumed, affecting the ballistic coefficient. It can be seen from Figure 14, however, that this difference leads to slight changes in the aerothermodynamic loads. Figure 15 shows the landing dispersion. From this analysis, it is evident that the role of a proper evaluation of thruster performance is crucial for a safe re-entry of the system. The choice of the specific landing point in the Pacific Ocean, considered in this work, allows for a margin higher than 2000 km from the nearest coast, enhancing the safety of such an uncontrolled demonstration mission.

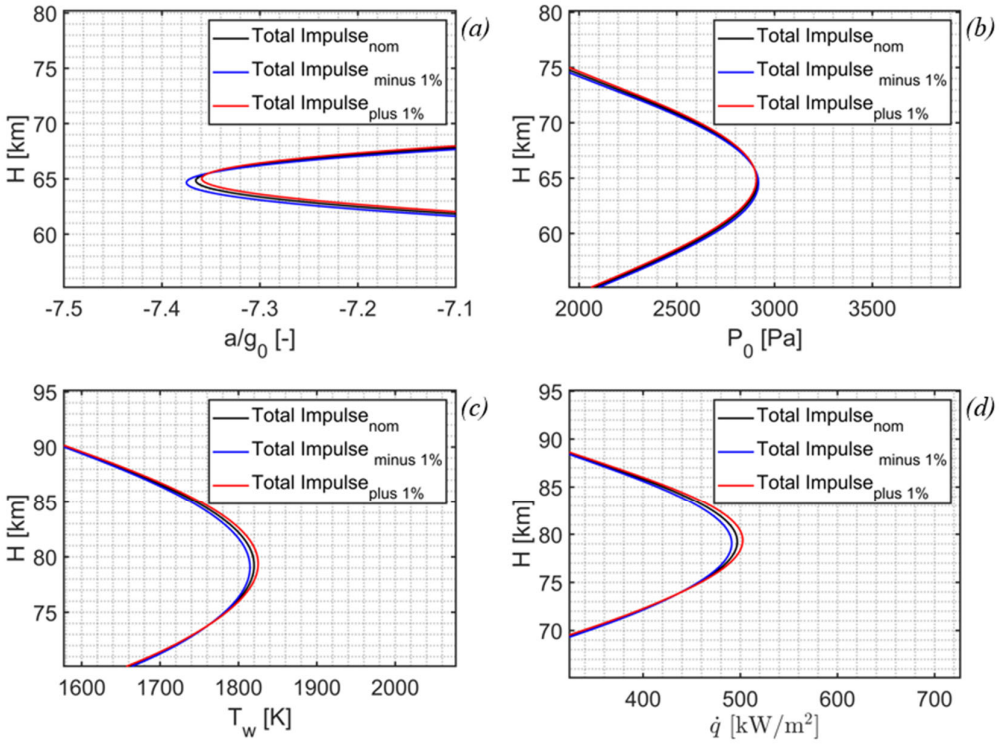


Figure 14. Trend of aerothermodynamic loads during re-entry; (**a**) accelerations, (**b**) pressures, (**c**) temperature, (**d**) heat flux (for different total impulse applied).

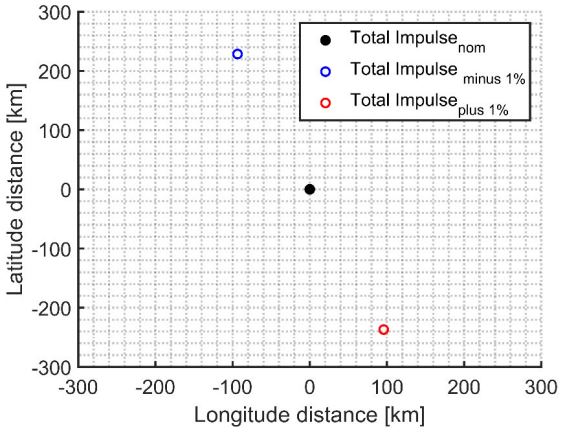


Figure 15. Landing dispersion obtained due to errors on total impulse applied (+/−1% in km).

3.4.5. Monte Carlo Analysis for Landing Dispersion in Propulsive Re-Entry

A Monte Carlo analysis, simulating 200 re-entries, was conducted using GMAT to evaluate landing dispersion and aerothermodynamic loads. This was accomplished by varying the C_D, the instant of thruster ignition, and the atmosphere density scale factor. It was imposed that each parameter varies as a Gaussian distribution, with their respective mean and variance values reported in Table 7. Uncertainties related to the total impulse were not considered, as it is assumed that the propulsion system provides nominal performance.

Table 7. Data on the distributions considered for the involved quantities.

	μ	**3σ**
C_D	C_D profile (Figure 5a)	0.1
t ignition	17,005 s	10 s
Atmosphere density scale factor	1	0.1

Figure 16 shows the results of Monte Carlo analysis related to landing dispersion and maxima of aerothermodynamic loads.

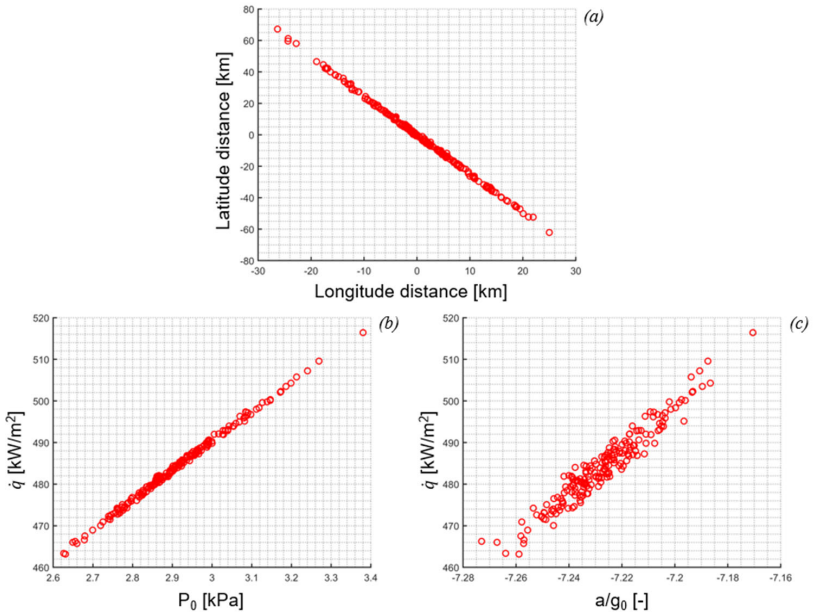


Figure 16. Landing dispersion (**a**), range of maximum pressure maximum load factor and maximum heat flux (**b**,**c**) values obtained from Monte Carlo analysis.

3.4.6. Influence of Radius of Curvature on Maximum Wall Temperature and Maximum Heat Flux

In this preliminary design, a radius of curvature of 0.3 m was selected, which results in a relatively high wall temperature and heat flux. As illustrated in Figure 17, a value of 0.4 m or 0.5 m was considered to reduce peak wall temperature and heat flux, starting from the thermal loads obtained in the nominal propulsive re-entry scenario.

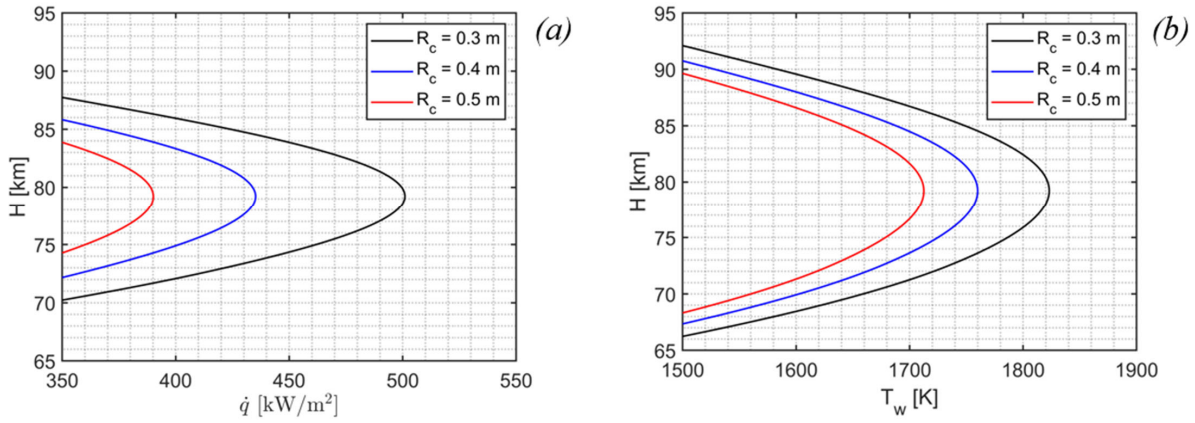


Figure 17. Thermal loads trend in propulsive re-entry for different radius of curvature: (**a**) heat flux, (**b**) wall temperature.

3.5. Conceptual Design of Monopropellant Propulsion System for the Propulsive Re-Entry

Based on the previous results, to address the uncertainties associated with drag coefficient and atmospheric density, which significantly influence the duration of the descent phase and the landing point, it was deemed advantageous to utilize a propulsive system. To demonstrate the feasibility of the concept and provide a preliminary configuration, in this section, the results of the design procedure described above, for a weighting percentage of 91% of Hydrogen Peroxide and a chamber pressure of 10 bar, are reported. A conical nozzle with an efficiency of 98% (with a convergence angle of 45° and a divergence angle of 15°) and catalyst bed loading (CBL) equal to 200 (kg·m^2)/s [25] were assumed. The mission requirements are derived from the study previously reported (Total impulse 3100 N s), and the imposed geometrical constraints for each configuration are reported in Table 8.

Table 8. Geometrical constraints imposed for each configuration (the symbol "/" indicate no constraints applied).

Design Constraint Input	Configuration 1	Configuration 2	Configuration 3
Maximum volume height	250 mm	250 mm	250 mm
Maximum volume diameter	350 mm	350 mm	350 mm
Distance between components	50 mm	50 mm	50 mm
Gas pressurization tank diameter	300 mm	/	/
H_2O_2 tank diameter	300 mm	300 mm	300 mm
Minimum allowed lateral distance between tanks and the constrained design volume	/	25 mm	/
Distance between pressurized hollow tanks and thruster	/	50 mm	/
Distance between z-axes of two spheres	/	/	80 mm

In Tables 9 and 10, mass data, the dimensions of all the parts of the thruster, and a summary of performance are given. It is observed that for the same chamber pressure in the three configurations, the mass of the engine subsystems decreases as the expansion ratio increases (related to the enhancement of performance that causes a decrease in mass flow rate). In particular, when evaluating the total mass components, the increase in nozzle mass (due to increase in expansion ratio and length) does not overlap with the apparent reductions in the mass of the high-test peroxide (HTP) and pressurization gas in this particular analysis. As the expansion ratio changes, the pipeline mass remains constant since the components are assumed to remain the same. To simplify manufacturing, the wall thickness was increased to 2 mm, even though the calculated thickness meeting the safety criteria was less than 1 mm.

Component masses were calculated for this thickness. Possible lay-outs are shown in the following figures (Figure 18): sequential arrangement of components, sequential arrangement with toroidal tank around the nozzle, and optimized distribution using the spherical tanks for pressurized gas. From the possible lay-out, the configuration with spherical tanks emerges as the best choice. A 10% margin was included in the mass estimation to account for elements whose mass is not known at this stage of the design. The tool automatically generates .stp files that can then be manipulated by software such as CATIA and Solid Works.

Table 9. Geometrical and masses characteristic of monopropellant thruster.

Quantity	Configuration 1	Configuration 2	Configuration 3
Optimum expansion ratio Ae/At	34	54	124
Diameter of gas-pressurized tank [mm]	300	271	91.62
Length of gas-pressurized tank [mm]	35.11	60.61	/
Diameter of H_2O_2 tank [mm]	300	300	300
Length of H_2O_2 tank [mm]	17.74	17.39	16.91
Nozzle external diameter [mm]	35.76	44.63	66.69
Diameter of catalytic chamber [mm]	14.13	14	13.79
Nozzle throat diameter [mm]	6.13	6.07	5.98
Length of catalytic chamber [mm]	27.84	27.84	27.84
Thruster total length [mm]	95.82	112.35	153.52
Nozzle divergent length [mm]	55.29	71.94	113.28
Nozzle convergent length [mm]	3.99	3.95	3.90
Nozzle mass [g]	31.62	48.74	107.4
Mass of pipeline [g]	20.1	20.1	20.1
Mass of retainer plate [g]	1.16	1.13	1.08
Mass of H_2O_2 tank [g]	313.85	307.7	299.3
Mass of H_2O_2 (+ 10% margin) [g]	2138.7	2096.7	2039.7
Mass of pressurized tank [g]	418.3	410	398.92
Mass of Nitrogen [g]	90.36	88.58	86.172
Catalytic chamber mass [g]	16.97	16.78	16.5
Total mass [g]	3032	2990	2970

Table 10. Summary of thruster performance.

Quantity	Configuration 1	Configuration 2	Configuration 3
Mass flow rate [g/s]	31.36	30.74	29.9
H_2O_2 Mass consumption [g]	1944.32	1905.88	1854
Chamber pressure [bar]	10	10	10
N_2 tank pressure [bar]	20.7	20.7	20.7
Total impulse [Ns]	3100	3100	3100
Cf	1.72	1.75	1.81
Specific impulse [s]	165.4	168.5	173.4

As can be observed in Table 7, the masses of the three configurations are comparable. Given the inherent uncertainties associated with the design procedure (with a 10% margin of error), the discrepancy between the best and worst configuration (between configurations 1 and 3, approximately 60 g) may not be significant. However, as illustrated in Table 8, configuration 3 exhibits the highest specific impulse. From these observations, it is recommended that configuration 3 be utilized. In conclusion, the specific impulse values are significantly higher than those considered in the mission analysis, which can be assumed to be conservative.

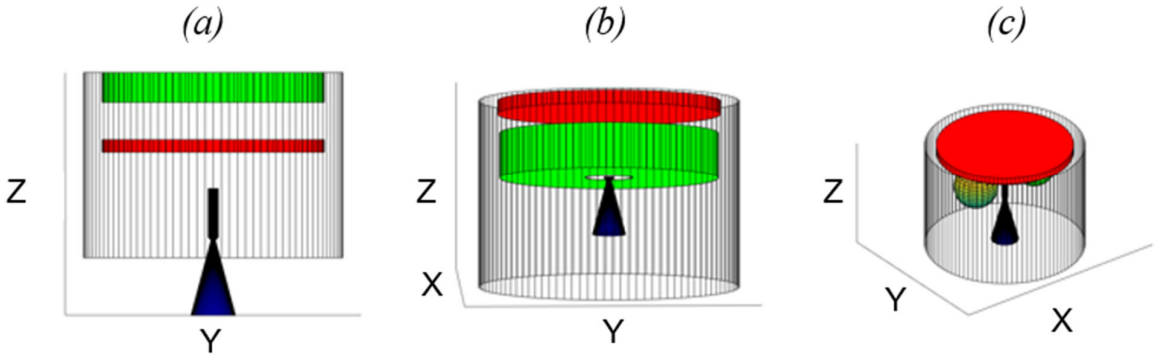


Figure 18. Configuration 1 (**a**) sequential layout: in red H_2O_2 tank, in green gas-pressurized tank, in blue the thrust chamber. Configuration 2 (**b**) sequential layout with toroidal tank of pressurization gas all around the thrust chamber: in red H_2O_2 tank, in green gas-pressurized tank, in blue the thrust chamber. Configuration 3 (**c**) spherical pressurized gas tanks: in red H_2O_2 tank, in green gas-pressurized tank, in blue the thrust chamber.

4. Conclusions

This paper presents an investigation into the re-entry dynamics of a satellite equipped with a propulsion system and a deployable aerobrake. The utilization of propulsive thrust for descent affords the benefit of shortened descent durations. Consequently, under equivalent uncertainties in critical parameters such as drag coefficient and atmospheric density, the satellite's landing location remains unaffected by factors such as Earth's rotation, solar activity, and geomagnetic influences, all of which influence atmospheric density. However, there are no noticeable differences in aerothermodynamic loads between the two types of re-entry. The descent time of an aerodynamically de-orbiting satellite can vary by $+/-3$ days due to $\pm 10\%$ changes in density and/or drag coefficient. As a result, the satellite may follow a ground-track that deviates from the nominal one, leading to extended dispersion. Conversely, employing a propulsive system mitigates the impact of uncertainties on descent duration, enabling the satellite to closely adhere to the intended ground-track. In this work, a non-impulsive application of the burn was considered, which

affects the dynamics of the satellite and causes the change of the landing point. The application of the DSMC method enabled the derivation of a plausible drag coefficient (C_D) profile as a function of altitude for this application. The stability analysis revealed a wide range in which the pitching moment derivative $C_{M_\alpha} < 0$ is negative, both in the folded and deployed configurations, ensuring that, in a preliminary design, phase lift force may be neglected, as the capsule automatically stabilizes around a null angle of attack.

Additionally, a tool was introduced for the preliminary design of a monopropellant thruster, facilitating the sizing of all components to adhere to the geometric dimensional constraints of the satellite. This tool independently assesses performance without reliance on external software such as CEA. Through optimization procedures, the optimal expansion ratio was identified among viable options meeting mission requirements, considering factors such as size and mass. Three potential layouts were examined, with the configuration featuring spherical pressurized gas tanks demonstrating superior performance. The tool's future enhancements may encompass the incorporation of propulsion units with multiple nozzles, catering to diverse mission objectives beyond those presented in this study, such as those employing monopropellant rockets for attitude control systems. Prospective developments may include the possibility of implementing sophisticated controls to further reduce dispersion during landing.

Author Contributions: Conceptualization, A.S., S.C. and S.M.; Methodology, A.S. and S.C.; Software, A.S. and D.D.P.; Validation, D.D.P.; Investigation, A.S.; Resources, R.S.; Data curation, A.S. and D.D.P.; Writing—original draft, A.S.; Writing—review & editing, S.C. and S.M.; Supervision, S.M., A.C. and R.S.; Project administration, R.S.; Funding acquisition, R.S. All authors have read and agreed to the published version of the manuscript.

Funding: This study was carried out within the Space It Up project funded by the Italian Space Agency, ASI, and the Ministry of University and Research, MUR, under contract n. 2024-5-E.0–CUP n. I53D24000060005.

Data Availability Statement: The original contributions presented in the study are included in the article, further inquiries can be directed to the corresponding author.

Conflicts of Interest: The authors declare no conflicts of interest.

Nomenclature

$\boldsymbol{a}$	Acceleration [m/s^2]
$\boldsymbol{N_A}$	Avogadro's number
$\boldsymbol{B}$	Ballistic parameter [kg/m^2]
$\boldsymbol{k_B}$	Boltzmann constant
t_b	Burning time [s]
CBL	Catalyst Bed Loading [kg·m^2/s]
$\boldsymbol{R_c}$	Curvature radius [m]
DSMC	Direct Simulation Monte Carlo
$\boldsymbol{S}$	Drag area [m^2]
$\boldsymbol{C_D}$	Drag coefficient [-]
c	Effective exhaust velocity [m/s]
E_i	Energy of the incident particle
E_r	Energy of the re-emitted particle
E_w	Energy the particle needs to deplete to reach thermal equilibrium with the Wall
$\boldsymbol{N_\infty}$	Free stream number density [m^{-3}]

R	Gas constant [J/mol K]
g_0	Gravitational constant [m/s^2]
c_p	Heat transfer coefficient [J/kg K]
C_L	Lift coefficient [-]
LEO	Low Earth Orbit
m	Mass [kg]
$\dot{m}$	Mass flow rate [kg/s]
B^*	Modified ballistic parameter [1/m]
C_p	Pressure coefficient [-]
d_{ref}	Reference molecular diameter [m]
$\dot{q}_0$	Stagnation point heat flux [W/m^2]
P_0	Stagnation point pressure [Pa]
T	Thrust [N]
I_{tot}	Total Impulse [N m]
ΔV	Velocity change [m/s]
V	Speed [m/s]
VLEO	Very Low Earth Orbit
T_w	Wall temperature [K]
α_{acc}	Accommodation coefficient [-]
α	Angle of attack [deg]
ρ	Atmospheric density [kg/m^3]
ϵ	Emissivity [-]
λ_∞	Free stream mean free path [m]
σ	Stefan-Boltzman constant [W/m^2 K^4]

References

1. IAA, Study Group on Cost Effective Earth Observation Missions. *IAA Position Paper on Cost effective Earth Observation Missions*; IAA: Paris, France, 2004.
2. Renga, A.; Gigantino, A.; Graziano, M.D.; Moccia, A.; Fedele, A.; Natalucci, S. Design considerations and performance analysis for RODiO distributed SAR mission. *Acta Astronaut.* **2023**, *210*, 474–482. [CrossRef]
3. Bassano, E.; Savino, R.; Richiello, C.; Russo, G.; Aurigemma, R.; Punzo, F. Irene-Italian re-entry nacelle for microgravity experiments. In Proceedings of the 62nd International Astronautical Congress, Cape Town, South Africa, 2 October 2011.
4. Punzo, F.; Ruggiero, M.; Aurigemma, R.; Dell'Aversana, P.; Gramiccia, L.; Vernillo, P.; Gardi, R.; Fedele, A.; Savino, R.; Mungiguerra, S.; et al. Development and flight test of a suborbital re-entry demonstrator. In Proceedings of the 72nd International Astronautical Congress (IAC), Dubai, United Arab Emirates, 25–29 October 2021.
5. Okolo, W.; Margolis, B.; D'Souza, S.; Barton, J. Development and Comparison of Control Architectures for a Mechanically Deployed Entry Vehicle. In Proceedings of the AIAA SciTech 2020 Forum, Orlando, FL, USA, 6–10 January 2020; p. 2012. [CrossRef]
6. Alunni, A.; D'Souza, S.N.; Yount, B.; Okolo, W.; Nikaido, B.; Margolis, B.; Johnson, B.J.; Hibbard, K.; Barton, J.; Lopez, G.; et al. Pterodactyl: Trade study for an integrated control system design of a mechanically deployed entry vehicle. In Proceedings of the AIAA SciTech 2020 Forum, Orlando, FL, USA, 6–10 January 2020; p. 1014. [CrossRef]
7. Olave, D.R.; Jara, N.C.; Palharini, R.C.; Palharini, R.S.A.; Gaglio, E.; Savino, R. Inflatable aerodynamic decelerator for CubeSat reentry and recovery: Altitude effects on the flowfield structure. *Aerosp. Sci. Technol.* **2023**, *138*, 108358. [CrossRef]
8. Jara, N.C.; Olave, D.R.; Palharini, R.C.; Gaglio, E.; Palharini, R.S.A.; Savino, R. Inflatable aerodynamic decelerator for CubeSat reentry and recovery: IAD geometrical effects on the flowfield structure. *Aerosp. Sci. Technol.* **2023**, *141*, 108571. [CrossRef]
9. Caqueo, N.; Palharini, R.C.; Palharini, R.S.A.; Gaglio, E.; Savino, R. Inflatable aerodynamic decelerators for CubeSat reentry and recovery: Surface properties. *Aerosp. Sci. Technol.* **2024**, *149*, 109151. [CrossRef]
10. Mungiguerra, S.; Gardi, R.; Savino, R.; Vernillo, P.; Ferracina, L.; Punzo, F.; Ruggiero, M.; Aurigemma, R.; Dell'aversana, P.; Gramiccia, L.; et al. Mini-IRENE, a Successful Re-entry Flight of a Deployable Heatshield Capsule. *Aerotec. Missili Spaz.* **2024**. [CrossRef]
11. Litteken, D.A. *Inflatable Technology: Using Flexible Materials to Make Large Structures*; NASA Technical Reports Server: Washington, DC, USA, 2019.
12. Hughes, S.J.; Cheatwood, F.M.; Dillman, R.A.; Calomino, A.M. Inflatable Re-entry Vehicle Experiment (IRVE)—4 Overview. NASA Technical Reports Server: Washington, DC, USA, 2011.

13. Chen, J. Aerodynamic Analysis of Deorbit Drag Sail for CubeSat Using DSMC Method. *Aerospace* **2024**, *11*, 315. [CrossRef]
14. Bird, G.A. *Molecular Gas Dynamics and the Direct Simulation of Gas Flows*; Clarendon: Oxford, UK, 1994.
15. Gaglio, E.; Guida, R.; Cecere, A.; Mungiguerra, S.; Savino, R. Assessment of a deployable aerodynamic control system for microsatellites recovery. In Proceedings of the 73rd International Astronautical Congress, Paris, France, 18–22 September 2022.
16. Fedele, A.; Mungiguerra, S. Aerodynamics and Flight Mechanics activities for a suborbital flight test of a deployable heat shield capsule. *Acta Astronaut.* **2018**, *151*, 324–333. [CrossRef]
17. Zamprotta, A.; Fedele, A.; Mungiguerra, S.; Savino, R. Study on Aerodynamic Stability of a Deployable Aerobraking Re-entry Capsule. In Proceedings of the 8th European Conference for Aeronautics and Space Sciences (EUCASS), Madrid, Spain, 1–4 July 2019. [CrossRef]
18. Mungiguerra, S.; Zuppardi, G.; Savino, R. Rarefied aerodynamics of a deployable re-entry capsule. *Aerosp. Sci. Technol.* **2017**, *69*, 395–403. [CrossRef]
19. Nagata, Y. Development and Flight Result of Nanosatellite BEAK for Demonstration of Nano-Size Planetary Atmospheric Probe Technology, ISAS Space Science Colloquium & Space Science Seminar. 2024. Available online: https://www.isas.jaxa.jp/researchers/colloquium/003873.html (accessed on 12 December 2024).
20. TechEdSat-4: Nano-Satellite Series-Technologies for Passive Reentry, Future Sample Return and Mars Missions. 2015. Available online: https://www.nasa.gov/wp-content/uploads/2022/01/techedsat4-508-13april2015.pdf (accessed on 5 May 2024).
21. Manente, M.; Trezzolani, F.; Magarotto, M.; Fantino, E.; Selmo, A.; Bellomo, N.; Toson, E.; Pavarin, D. REGULUS: A propulsion platform to boost small satellite missions. *Acta Astronaut.* **2019**, *157*, 241–249. [CrossRef]
22. Sutton, G.; Biblarz, O. *Rocket Propulsion Elements*, 7th ed.; John Wiley & Sons: Hoboken, NJ, USA, 2001.
23. Cassese, S.; Mungiguerra, S.; Guida, R.; Cecere, A.; Savino, R. Regression Rate and Performance Analysis via Ballistic Reconstruction of a small-scale H_2O_2-based Hybrid Rocket fuelled by Polyvinyl Chloride. *Aerosp. Sci. Technol.* **2024**, *146*, 108911. [CrossRef]
24. Cassese, S.; Gallo, G.; Mungiguerra, S.; Cecere, A.; Savino, R. Preliminary Design and Study of 5N HTP Monopropellant Thruster for Nanosatellites. *Acta Astronaut.* **2022**, *202*, 94–103. [CrossRef]
25. Adami, A. Multidisciplinary Design Optimization of Hydrogen Peroxide Monopropellant Propulsion System using GA and SQP. *Int. J. Comput. Appl.* **2015**, *113*, 14–21. [CrossRef]
26. Plimpton, S.; Moore, S.; Borner, A.; Stagg, A.; Koehler, T.; Torczynski, J.; Gallis, M. Direct simulation monte carlo on petaflop supercomputers and beyond. *Phys. Fluids* **2019**, *31*, 086101. [CrossRef]
27. Hughes, S.P. General Mission Analysis Tool (GMAT), User Guide. 2007. Available online: https://ntrs.nasa.gov/api/citations/20080047410/downloads/20080047410.pdf (accessed on 5 May 2024).
28. Fujita, K. Air Intake Performance of Air Breathing Ion Engines. *J. Jpn. Soc. Aeronaut. Space Sci.* **2005**, *52*, 514–521. [CrossRef]
29. Jiang, Y.; Zhang, J.; Tian, P.; Liang, T.; Li, Z.; Wen, D. Aerodynamic drag analysis and reduction strategy for satellites in Very Low Earth Orbit. *Aerosp. Sci. Technol.* **2023**, *132*, 108077. [CrossRef]
30. Maxwell, J.C. VII. on stresses in rarified gases arising from inequalities of temperature. *Philos. Trans. R. Soc. Lond.* **1879**, *170*, 231–256.
31. Livadiotti, S.; Crisp, N.H.; Roberts, P.C.; Worrall, S.D.; Oiko, V.T.; Edmondson, S.; Haigh, S.J.; Huyton, C.; Smith, K.L.; Sinpetru, L.A.; et al. A review of gas-surface interaction models for orbital aerodynamics applications. *Prog. Aerosp. Sci.* **2020**, *119*, 100675. [CrossRef]
32. Carandente, V.; Zuppardi, G.; Savino, R. Aerothermodynamic and stability analyses of a deployable re-entry capsule. *Acta Astronaut.* **2014**, *93*, 291–303. [CrossRef]
33. Anderson, J.D. *Hypersonic and High Temperature Gas Dynamics*; McGrow-Hill Book Company: New York, NY, USA, 1989.
34. Tauber, M.E. *A Review of High Speed Convective, Heat Transfer Computation Methods*; NASA Technical Paper; NASA: Washington, DC, USA, 1989; p. 2914.
35. Carandente, V.; Savino, R. New Concepts of Deployable De-Orbit and Re-Entry Systems for CubeSat Miniaturized Satellites. *Recent Pat. Eng.* **2014**, *8*, 2–12. [CrossRef]
36. Gordon, S.; McBride, B.J. *Computer Program of Complex Chemical Equilibrium Compositions and Applications*; NASA Reference Publication: Washington, DC, USA, 1994; p. 1311.
37. Bowker, M. *The Basis and Applications of Heterogeneous Catalysis*; Oxford University Press: New York, NY, USA, 1998.
38. Humble, R.W. *Space Propulsion Analysis and Design*; Mc Graw-Hill: New York, NY, USA, 1995.
39. Cervone, A.; Torre, L.; d'Agostino, L.; Musker, A.J.; Roberts, G.T.; Bramanti, C.; Saccoccia, G. Development of hydrogen peroxide monopropellant rockets. In Proceedings of the Collection of Technical Papers—AIAA/ASME/SAE/ASEE 42nd Joint Propulsion Conference, Sacramento, CA, USA, 9–12 July 2006; pp. 8786–8796. [CrossRef]
40. Department, C.C.E. Flow of Fluids Through Valves, Fittings, and Pipe. In *Crane Valves*; Crane Co.: New York, NY, USA, 2001; Available online: https://www.researchgate.net/profile/Brian-Hanley-6/post/How-to-calculate-the-Nitrogen-flowrate-knowing-pressure-in-pipe-line-and-pipe-diameter/attachment/59d63db579197b807799a767/AS:

421054863429633@1477398710366/download/Flow+of+Fluids+-+Through+Valve,+Fittings+and+Pipes.pdf (accessed on 5 April 2024).
41. Berthet, M.; Yamada, K.; Nagata, Y.; Suzuki, K. Feasibility assessment of passive stabilisation for a nanosatellite with aeroshell deployed by orbit-attitude-aerodynamics simulation platform. *Acta Astronaut.* **2020**, *173*, 266–278. [CrossRef]
42. Silvestroni, L.; Mungiguerra, S.; Sciti, D.; Di Martino, G.D.; Savino, R. Effect of hypersonic flow chemical composition on the oxidation behavior of a super-strong UHTC. *Corros. Sci.* **2019**, *159*, 108125. [CrossRef]
43. Fedele, A.; Omar, S.; Cantoni, S.; Savino, R.; Bevilacqua, R. Precise re-entry and landing of propellantless spacecraft. *Adv. Space Res.* **2021**, *68*, 4336–4358. [CrossRef]
44. Desai, P.N.; Braun, R.D.; Powell, R.W.; Engelund, W.C.; Tartabini, P.V. Six-degree-of-freedom entry dispersion analysis for the meteor recovery module. *J. Spacecr. Rocket.* **1997**, *34*, 334–340. [CrossRef]
45. Desai, P.N.; Cheatwood, F.M. Entry dispersion analysis for the genesis sample return capsule. *J. Spacecr. Rocket.* **2001**, *38*, 345–350. [CrossRef]
46. Desai, P.N.; Lyons, D.T.; Tooley, K. Entry, descent, and landing operations analysis for the stardust entry capsule. *J. Spacecr. Rocket.* **2008**, *45*, 1262–1268. [CrossRef]
47. Cercignani, C.; Lampis, M. Kinetic models for gas-surface interactions. *Transp. Theory Stat. Phys.* **1971**, *1*, 101–114. [CrossRef]
48. Lord, R. Some extensions to the cercignani–lampis gas–surface scattering kernel. *Phys. Fluids A Fluid Dyn.* **1991**, *3*, 706–710. [CrossRef]
49. Lord, R. Some further extensions of the cercignani–lampis gas–surface interaction model. *Phys. Fluids* **1995**, *7*, 1159–1161. [CrossRef]
50. Hedahl, M.O.; Wilmoth, R.G. *Comparisons of the Maxwell and cll Gas/Surface Interaction Models Using dsmc*; NASA Langley Research Center: Hampton, VA, USA, 1995. Available online: https://ntrs.nasa.gov/api/citations/19970003075/downloads/19970003075.pdf (accessed on 5 May 2024).

Disclaimer/Publisher's Note: The statements, opinions and data contained in all publications are solely those of the individual author(s) and contributor(s) and not of MDPI and/or the editor(s). MDPI and/or the editor(s) disclaim responsibility for any injury to people or property resulting from any ideas, methods, instructions or products referred to in the content.